Chinese Chemical Letters 33 (2022) 1141–1153

Contents lists available at ScienceDirect

Chinese Chemical Letters

journal homepage: www.elsevier.com/locate/cclet

Recent research progress of bimetallic phosphides-based nanomaterials as cocatalyst for photocatalytic hydrogen evolution

Chunmei Li[a], Daqiang Zhu[a], Shasha Cheng[a], Yan Zuo[a], Yun Wang[a,*], Changchang Ma[b], Hongjun Dong[a,*]

[a] Advanced Chemical Engineering Laboratory of Green Materials and Energy of Jiangsu Province, Institute of Green Chemistry and Chemical Technology, School of Chemistry and Chemical Engineering, Jiangsu University, Zhenjiang 212013, China
[b] Department of Chemistry, Dongguk University, Seoul 04620, Republic of Korea

ARTICLE INFO

Article history:
Received 28 April 2021
Revised 19 June 2021
Accepted 26 July 2021
Available online 30 July 2021

Keywords:
Bimetallic Phosphides
Cocatalyst
Photocatalysis
Hydrogen evolution
Dye Sensitization Effect

ABSTRACT

Hydrogen energy (H_2) has been considered as the most possible consummate candidates for replacing the traditional fossil fuels because of its higher combustion heat value and lower environmental pollution. Photocatalytic hydrogen evolution (PHE) from water splitting based on semiconductors is a promising technology towards converting solar energy into sustainable H_2 fuel evolution. Developing high-activity and abundant source semiconductor materials is particularly important to realize highly efficient hydrogen evolution as for photocatalysis technology. However, unmodified pristine photocatalysts are often unable to overcome the weakness of low performance due to their limitations. In recent years, transition metal phosphides (TMPs) were used as valid co-catalysts to replace the classic precious metal materials in the process of photocatalytic reaction owing to their lower cost and higher combustion heat value. What is more, bimetallic phosphides have been also caused widespread concern in H_2 evolution reaction owing to its much lower overpotential, more superior conductivity, and weaker charge carriers transfer impedance in comparison to those of single metal phosphides. In this minireview, we concluded the latest developments of bimetallic phosphides for a series of photocatalytic reactions. Firstly, we briefly summarize the present loading methods of bimetallic phosphides (BMPs) anchored on the photocatalyst. After that, the H_2 evolution efficiency based on BMPs as cocatalyst is also studied in detail. Besides, the application of BMPs-based host photocatalyst for H_2 evolution under dye sensitization effect has also been discussed. At last, the current development prospects and prospective challenges in many ways of BMPs are proposed. We sincerely hope this minireview has certain reference value for great developments of BMPs in the future research.

1. Introduction

Into the 21st century, the energy problem has become more and more serious with the rapid development of economy. It is crucial to exploit the renewable and green non-pollution new-type energy sources to replace fossil fuels for alleviating the current energy crisis. Hydrogen energy (H_2) has been considered as the most promising candidate due to its unique advantages, such as high calorific value and fuel efficiency, zero pollution emission as well as ease to storage and transportation [1–6]. Among the reported technologies towards H_2 evolution in recent decades, photocatalytic hydrogen evolution (PHE) based on semiconductor materials from water splitting has been deemed to the most potential technology, which can directly utilize solar energy as a driving force to generate chemical energy H_2 [7–12]. With regards to photocatalysis technology, it is very important to single out appropriate semiconductor photocatalyst with ideal catalytic activity, perfect photostability and easy synthesis characters. The reported photocatalysts at present mainly include non-metallic material ($g\text{-}C_3N_4$) [13–15] metal sulfide [16–18], metallic oxide [19–21], metal-organic frameworks [22,23], and so on. Nevertheless, there are still many disadvantages in the PHE reaction process resulting in activity declines and large-scale H_2 evolution, including lower energy utilization efficiency, higher photo-generated charge carrier recombination rate, lack of surface-active sites and so on. In the current stage of photocatalytic technology development, exploiting the new photocatalysts with high-efficiency and stability is relatively difficult. Hence, researchers have devoted themselves to

* Corresponding authors.
E-mail addresses: yunwang@ujs.edu.cn (Y. Wang), donghongjun6698@aliyun.com (H. Dong).

https://doi.org/10.1016/j.cclet.2021.07.057
1001-8417/

working on modifying the existing photocatalysts to improve their photocatalytic activity for practical applications.

So far, various modification strategies have been developed and utilized, such as morphological control [24–26], cocatalyst loading [27–29], ion or group doping [30,31], dye sensitization [32,33], hetero/homojunction construction [34–36]. Among them, loading cocatalysts have obtained more attention because they can improve light absorbability and broaden the range of light absorption, accelerating the transport and separation of charge carriers as well as providing abundant surface reactive active site for water reduced to H_2 [37,38]. In the past decades, transition metal phosphides (TMPs) served as satisfactory cocatalyst to replace high-cost and low-abundance noble metal in PHE reaction system have brought about widespread attention due to their unique advantages, including zero-valent metallic feature, less overpotential, good electric conductivity, facile release of H_2, inherent structural stability, cost-effectiveness and so on [39–42]. Inspired by these, our group developed a variety of photocatalysts based on TMPs as cocatalyst in PHE reaction system. For example, we prepared the CoP/g-C_3N_4 photocatalyst through embellishing CoP nanodots on the g-C_3N_4 surface, the characteristic P(δ^-)-Co(δ^+)-N(δ^-) surface state of which results in the superior PHE activity of 96.2 μmol/h, which is nearly three times as high than that of Pt/g-C_3N_4 photocatalyst [43]. Besides, we also constructed 0D/2D heterojunction through decorating Ni_2P quantum dots on the surface of g-C_3N_4 nanosheet, which remarkably enhanced the PHE and photoelectrochemical activities under visible light [44]. As the derivative of TMPs, bimetallic phosphides (BMPs) have caught the attention of scientific research workers due to adjustable electronic structure, good electronic conductivity, much lower H_2 evolution overpotential and small charge carriers transfer impedance in contrast to the relevant single metal phosphides [45–48]. Specifically, bimetallic atoms possess a much higher positive charge, which can significantly increase the receptive active sites amount of hydride ions. Synchronously, the P charged atoms with much negatively can capture protons effectively by electrostatic suction capacity, contributing to the promotion of photocatalytic activity [49,50]. Furthermore, it is known that the photocatalytic property is closely relevant to the surface character and electronic structures of semiconductor materials. It is relatively easier for BMPs to implement that adding the surface-active sites amount for electron acceptors and optimizing the electronic structure by means of rationally tuning composition of bimetal ions [51–53]. Besides, as the cocatalyst in the PHE system, the multiple active ingredients of BMPs not only can serve as photoelectron capture role for optimizing the surface H_2 evolution kinetics, but promote the separation and transmission of photogenerated charge carriers more effectively [54,55]. Therefore, BMPs should be able to the more potentially promising non-noble promotor for PHE from water splitting by contrast with mono-metallic phosphates. Many works have been investigated and conducted on such contents in recent years.

Hence, in this minireview, the recent research progress on BMPs as co-catalysts towards PHE from water splitting has been summarized. Firstly, we summarized the loading methods of BMPs on the semiconductor photocatalyst, mainly including mechanical mixture and in-situ solid-state phosphating method. Especially the recent development on BMPs as co-catalysts with different components in the field of photocatalysis is emphasized in this review. The host photocatalysts are mainly involved in g-C_3N_4, metal sulfide and metallic oxide. Afterward, we also discuss some potential reports for BMPs as host photocatalysts proceeding PHE reaction under the action of dye sensitization. Finally, the challenges and development prospects of BMPs in the domain of PHE are suggested. This minireview is desired to furnish a relatively appropriate analysis on current research results of BMPs. We hope this will be helpful for further in-depth studies in the future.

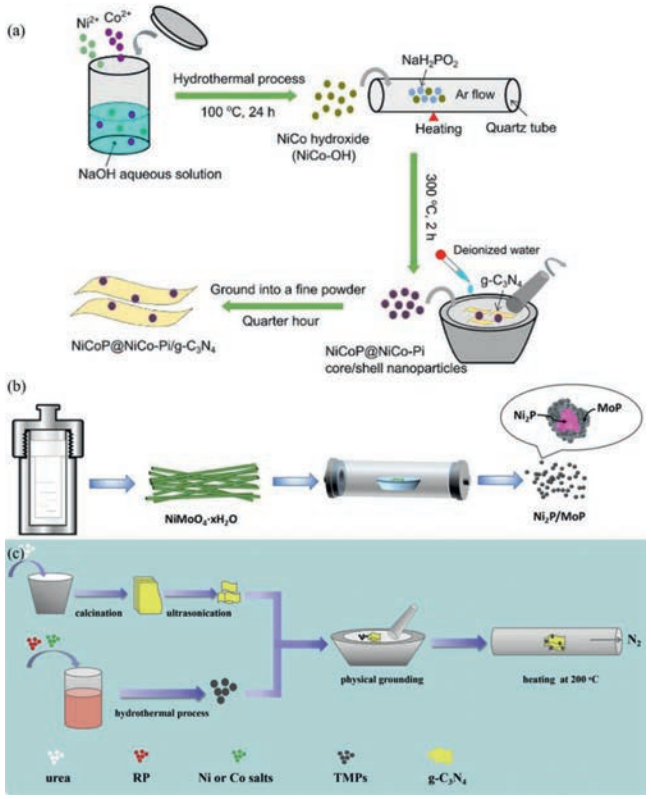

Fig. 1. Schematic of preparation process of NiCoP@NiCo-Pi/g-C_3N_4 (a), Copied with permission [58]. Copyright 2017, RSC; Ni_2P/MoP@ g-C_3N_4 (b), Copied with permission [59]. Copyright 2020, ACS; and TMPs/g-C_3N_4 (c). Copied with permission [60], Copyright 2019, Elsevier.

2. Synthetic or loading methods of BMPs as cocatalyst

2.1. Mechanical mixture loading method

The mechanical mixture has been regarded as one of the most common strategies to make the BMPs as cocatalysts loaded on the surface of semiconductor photocatalyst. In the loading procedure, the BMPs and semiconductors are first prepared respectively and then the two were combined by an extra mechanical mixture method, such as physical grinding, hydrothermal or solvothermal process [56,57]. As shown in Fig. 1a, NiCoP@NiCo-Pi/g-C_3N_4 with core/shell structure photocatalyst was prepared by the above method [58]. Firstly, NiCo-OH precursor was synthesized through the facile hydrothermal reaction, washing with deionized water and ethanol as well as vacuum drying process. After that, NiCoP@NiCo-Pi nanoparticles with core/shell structure were constructed through the reported phosphating process. Specifically, the quantitative NiCo-OH and NaH_2PO_2 precursors (molar ratio, Ni and Co to P is 1:5) were mixed well mechanically. Therewith, the mixed precursors had to go through the annealed process (300 °C, 2 h and the heating rate of 5 °C/min) and NiCoP@NiCo-Pi was obtained after washing and drying process. The g-C_3N_4 synthetic procedures are as follows: a certain amount of dicyandiamide and barbituric acid were well-distributed in distilled water and heated under stirring until the water has been evaporated. Next, the obtained white sample was through calcined (550 °C for 4 h), collected and grand procedure, the g-C_3N_4 sample was successful synthesis. At last, NiCoP@NiCo-Pi/g-C_3N_4 sample was prepared through a facile grinding method. The preparative g-C_3N_4 sample and NiCoP@NiCo-Pi with different weight percentages are thoroughly ground after dispersing in a small amount of deionized

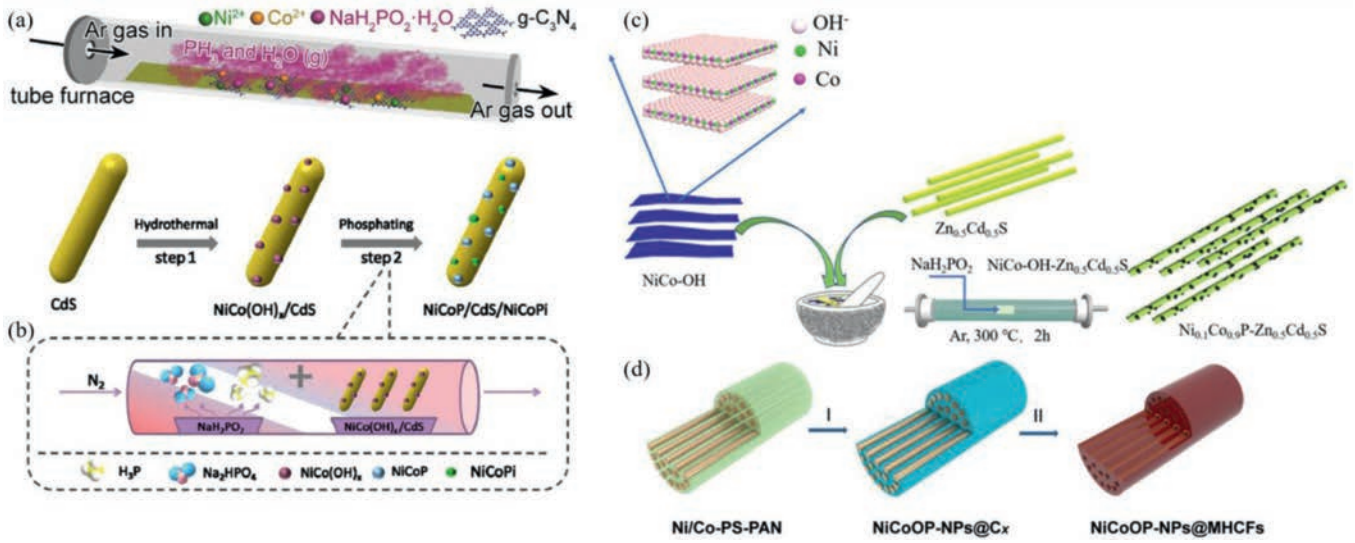

Fig. 2. Schematic representation of the synthetic route for (a) NiCoP/g-C_3N_4, Copied with permission [64]. Copyright 2019, Elsevier; (b) NiCoP/CdS/NiCoPi, Copied with permission [67]. Copyright 2019, ACS; (c) $Ni_xCo_{1-x}P/Zn_{0.5}Cd_{0.5}S$, Copied with permission [68]. Copyright 2019, Elsevier and (d) NiCoOP-NPs@MHCFs photocatalysts. Copied with permission [69]. Copyright 2019, Wiley-VCH.

water to enlarge their contact areas. Go through the above steps again and the core/shell NiCoP@NiCo-Pi nanoparticles were attached on the g-C_3N_4 surface after being dried under vacuum. Ma and co-workers also constructed the bimetal Ni_2P/MoP@ g-C_3N_4 photocatalysts in the light of this scheme. The specific synthesis methods are exhibited in Fig. 1b [59]. Besides, NiCoP anchored g-C_3N_4 nanosheets photocatalysts were prepared also according to the above method and just make some slight changes [60]. As illustrated in Fig. 1c, g-C_3N_4 nanosheets and NiCoP nanoparticles were synthesized through thermal polymerization and solvothermal methods, respectively. After that, NiCoP/g-C_3N_4 photocatalysts were prepared via physical grinding followed by calcination under N_2 atmosphere. Generally, this loading method has a positive effect on controlling the size and morphology of BMPs. But the interfacial contact between semiconductor photocatalyst and BMPs is rival ricketiness, which has a negative influence on the stability of photocatalyst for H_2 generation.

2.2. In-situ solid-state phosphating method

In-situ solid-state phosphating method also defined as electrostatic adsorption self-assembly loading method may be involved in the following synthesis process: Firstly, a certain amount of solid metal source is mingled with main catalyst in solution. After mixing homogeneous through stirring or ultrasonic process, the next step is steaming dry to remove solvents followed with thermal treatment in shielding gas with appropriate phosphorus source. After subsequent washing and drying treatment, the desired photocatalysts are obtained [61–63]. For example, Guo and co-workers synthesized the NiCoP/g-C_3N_4 photocatalyst through this typical synthesis procedure [64]. Firstly, the g-C_3N_4 nanosheets were acquired by the familiar polycondensation process. Then, the dispersed g-C_3N_4 powder in deionized water was mixed with a certain amount of Co and/or Ni saline aqueous solution under stirring and the subsequent ultrasonic reaction for 1h. After that, the mixed solution went through 80 °C water bath for 12 h for the purpose of the metal ions being absorbed on the surface of g-C_3N_4 powder. After that, the mixing g-C_3N_4 powder was ground together with $NaH_2PO_2{\cdot}H_2O$ finely. After executing the representative phosphating process under Ar flow (300 °C for 2 h) and the subsequent washing and drying process, the NiCoP/g-C_3N_4 photocatalyst was successfully prepared (shown in Fig. 2a). Furthermore, our group used this method to prepare a variety of composite photocatalyst based on BMPs as cocatalyst, including $Mn_{0.67}Co_{1.33}P$/g-C_3N_4 [65], Mo-Ni_2P/g-C_3N_4 [66] and so on. Besides g-C_3N_4 as main catalyst, other catalysts with BMPs as cocatalyst have also been reported. For instance, Zhao and co-workers prepared NiCoP/CdS/NiCoPi photocatalysts using the following methods [67]. As exhibited in Fig. 2b. CdS was firstly according to the previously reported hydrothermal synthesis method, there is no more introduction here. The quantitative CdS was dispersed in deionized water with cobalt(II) salt, nickel(II) salt, NH_4F and urea with a specific molar ratio. After that, the mixed solution was gone by hydrothermal treatment at 120 °C continuing 10 h to make the bimetal ions combined with CdS and get the $CdS/NiCo(OH)_x$ precursor. At last, the preparative precursor and a certain amount of phosphorus source (NaH_2PO_2) were treated at 300 °C in the 10 mL/min nitrogen flow for 2 h. In this process, NiCoP/CdS/NiCoPi photocatalysts were prepared by modulating the quantity of nickel-cobalt precursor. Furthermore, the individual NiCoP/CdS and NiCoPi/CdS photocatalyst was prepared through changing the temperature of the phosphating process (150 °C for 2 h in the 10 mL/min nitrogen flow) and the flow rate of carrier gas (40 mL/min), respectively. According to the similar approach, the $Ni_xCo_{1-x}P/Zn_{0.5}Cd_{0.5}S$ photocatalysts were also synthesized by the procedure in Fig. 2c and the x value is the ratio of added raw materials Ni^{2+} and Co^{2+} [68]. Furthermore, David, *et al.* prepared nickel cobalt oxyphosphide nanoparticles (NiCoOP NPs) restricted into the multichannel hollow carbon fibers (MHCFs) photochemical catalyst according to this method with some modifications. The integral synthesis process of the NiCoOP-NPs@MHCFs sample has been depicted in Fig. 2d [69]. The quantified $Co(Ac)_2{\cdot}4H_2O$, $Ni(Ac)_2{\cdot}4H_2O$, polystyrene (PS) and polyacrylonitrile (PAN) are dissolved in N,N-Dimethylformamide (DMF) solution firstly. After that, the preparative mixture was stirred constantly overnight at 65 °C to obtain a precursor solution. Through electrospinning process, the Ni/Co-PS-PAN fiber was prepared and stored at 70 °C. Then, Ni/Co-PS-PAN fiber and NaH_2PO_2 are annealed under an N_2 flow at 350 °C for 2 h (heating rate is 5 °C/min) to get NiCoOP-NPs@Cx fibers. At last, NiCoOP-NPs@MHCFs catalyst was obtained by the NiCoOP-NPs@Cx fibers annealed at 800 °C for 4 h in the N_2 flow (heating rate is also 5 °C/min). Through the in-situ solid-state

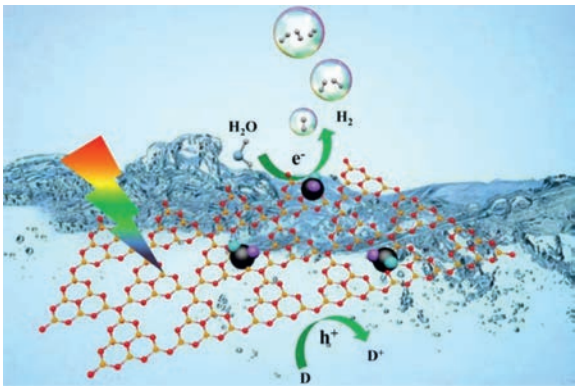

Fig. 3. The feasible PHE reaction paths simulation based on BMPs as cocatalysts and g-C_3N_4 for an example as main photocatalyst.

phosphating method can bring the BMPs cocatalysts and main photocatalyst in close contact for improving stability, it is relatively difficult to maintain size and shape of BMPs, which is disadvantageous to the improvement of photocatalytic activity owing to the reduction in the number of surface reactive active sites.

3. Application of BMPs in photocatalytic H_2 evolution

In its present form, developing new photocatalysts is a relative difficulty to significantly improve photocatalytic H_2 generation activity to alleviate the current global energy crisis. Therefore, modification of existing photocatalysts has been considered by researchers intensively in the past decades. Among the existing modification methods, the most common methods mainly include regulating morphology, doping element or group, constructing homo/heterojunction, loading cocatalysts and so forth. As for BMPs, they can often be used as a co-catalyst because of its inherent unique advantages. Recent insights mainly focus on BMPs cooperating with the host photocatalyst to acquire better H_2 evolution activity, including g-C_3N_4, metal sulfide, metallic oxide and so on. The feasible PHE reaction paths simulation is described as follows in Fig. 3 (g-C_3N_4 as an example): Firstly, in the sunshine condition, the electrons located on valence band (VB) of semiconductor photocatalyst are excited and transferred to conduction band (CB) for forming photogenerated charge carriers. The following is that the photoelectrons and holes are separated and migrated to the photocatalyst surface. Next, the photoelectrons are immediately captured by BMPs as reactive active site for reduction H_2O molecules to generate H_2. Meanwhile, the photogenerated holes are consumed ceaselessly by suitable sacrificial agents in water. In this reaction process, the BMPs can gather the photoelectrons to accelerate the separation of electron-hole pairs as well as act as surface reactive active site for producing H_2 from water splitting effectively. Furthermore, the coexistence of exclusively dual surface bonding states of BMPs could acquire more reaction-active sites for enhancing the PHE activity.

3.1. BMPs/g-C_3N_4 photocatalyst

In the past decades, as "brilliant" nonmetallic photocatalytic hydrogen evolution materials, g-C_3N_4 has been extensive and intensive researched because of its unique advantages, such as low price, high thermal and chemical stability, suitable band gap positions [70–72]. However, the PHE activity of pristine g-C_3N_4 is always not faultless owing to the inherently insufficient light absorption in visible-light region, fast photogenerated carrier recombination rate and dull surface reaction. It is indispensable to employ appropriate cocatalysts to dramatically boost the performance of g-C_3N_4 photocatalytic material. BMPs have been quite appealing attention as non-precious cocatalysts for PHE reaction over g-C_3N_4 attributing to its better electrical conductivity, lower overpotential for H_2 generation and smaller charge transfer impedance and more readily release H_2 from the surface-active sites than mono-metallic phosphates. For example, Xie and coworkers synthesized NiCoP/g-C_3N_4 photocatalyst by the facile one-pot strategy. It exhibits the optimal PHE rate of 1643 μmol h^{-1} g^{-1}, which is much superior by contrast with that of pure g-C_3N_4 [73]. This superior PHE performance is because of the enhanced transfer and separation efficiency of photoinduced charge carriers. Inspired by this work, our group prepared the 3D/2D NiCoP/g-C_3N_4 mesoporous heterostructure photocatalyst by means of the *in-situ* solid-state phosphating method (Fig. 4) [74]. The TEM images notarized that 3D mesoporous NiCoP nanoclusters were inbuilt on the 2D g-C_3N_4 nanosheets surfaces uniformly. Also, the mesoporous NiCoP nanocluster was composed of nanodots with the size of about 5-10 nm. This particular structural feature can act as a nanoreactor, which is conducive to the activation and diffusion of H_2O molecules and thus enhancing PHE activity. Besides, we prove the dual $Ni^{\delta+}-N^{\delta-}$ and $Co^{\delta+}-N^{\delta-}$ bonding states are taken shape on g-C_3N_4 surface by X-ray absorption near edge structure absorption spectra, which facilitated electron dissociation and transfer and thus boosting the stability of the prepared photocatalyst. As expected, the optimal PHE rates of the NiCoP/g-C_3N_4 is up to 71.5 μmol/h, which is higher than that of Pt/g-C_3N_4 and g-C_3N_4 samples. Furthermore, the PHE rate based on the NiCoP/g-C_3N_4 sample is also much higher than that of other different nickel-cobalt mole ratios samples. Additionally, the highest apparent quantum efficiency of the NiCoP/g-C_3N_4-3 photocatalyst is 4.8% at 420 nm. More noteworthy, the NiCoP/g-C_3N_4 sample revealed higher stability and reusability. This result proves this bonding form overcomes the shortcomings of metal phosphates as cocatalyst with effect.

In addition to NiCoP as ideal cocatalyst of g-C_3N_4, NiFeP as cocatalyst also exhibited the desired PHE performance under simulated solar light irradiation [75]. As exhibited in Fig. 5, the highest PHE rate NiFeP/g-C_3N_4 comes up to 3.549 mmol g^{-1} h^{-1} and the turnover frequency reached 10.4 h^{-1}. After three cycles PHE reaction, the activity over NiFeP/g-C_3N_4 sample has almost no reduction. Besides, the apparent quantum efficiency (AQE) values achieve 4.98% at 420 nm, which is slightly higher in contrast with that of NiCoP as cocatalyst (4.8%). It is worth noting that the NiFeP as co-catalyst was proved to reduce the ΔG_{H_2O} and ΔG_{H^*} in PHE reaction process by the density functional theory calculations, which also determines the electron directional migration pathway between the NiFeP and g-C_3N_4 interface. The above two are the main reasons for enhancing the PHE activity. Besides, 5 nm NiCoP nanoparticles and ZnNiP nanoblocks coupled with g-C_3N_4 as PHE photocatalyst have been reported and both showed high activity [76,55].

There are also some reports on ternary composite photocatalyst based on BMPs as cocatalyst in the g-C_3N_4 system. Li *et al.* prepared ternary g-C_3N_4–$NiCoP_2$–porous carbon (PC) heterostructure using metal organic framework (MOF) as a template [77]. As shown in Figs. 6a–c, MOF-derived $NiCoP_2$ and PC nanoparticles with the diameter of 10–20 nm are evenly distributed on the surface of g-C_3N_4 nanosheet without distinct agglomeration. The formation of 0D/2D composite heterostructure adds the surface reactive active site of g-C_3N_4 as well as enhances the transport and utilization of the charge carriers. Consequently, the prepared samples showed high PHE activity (Figs. 6d–h). And the optimal PHE rate is 48.3 μmol/h over g-C_3N_4–$Ni_{0.3}Co_{0.7}P_2$–PC sample (the NiP_2–PC content is 5 wt% and the Ni/Co molar ratio is 3:7) under UV-visible irradiation. The PHE activity over g-C_3N_4–$NiCoP_2$–PC is also apparently superior to that of g-C_3N_4–NiP_2–PC and g-C_3N_4

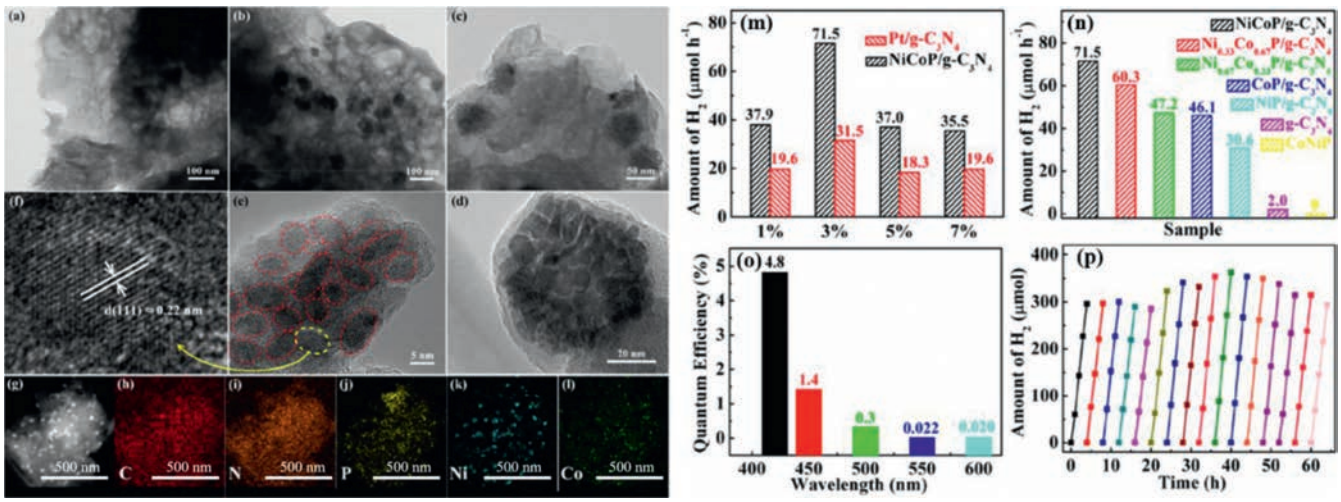

Fig. 4. TEM image of g-C_3N_4 (a) and NiCoP/g-C_3N_4 samples (b, c, d). HRTEM (e, f), HAADF (g), and EDX elemental mapping (h–l) images of NiCoP/ g-C_3N_4 sample. Various of PHE performance over the as-prepared different samples (m-p). Copied with permission [74]. Copyright 2020, ACS.

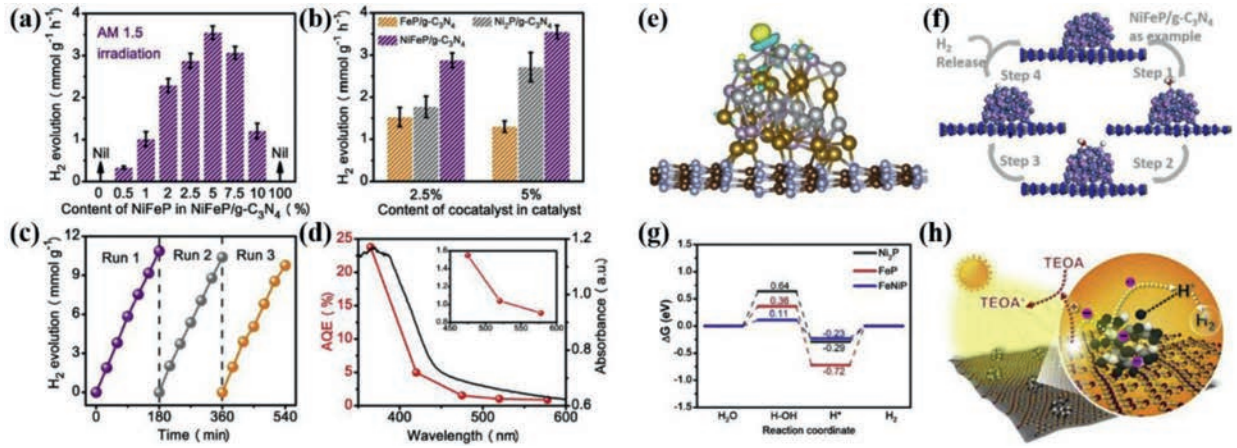

Fig. 5. The PHE performances for the prepared different photocatalysts (a-d). Local charge density difference (e), water adsorption models (f), free energy schemes for H_2O reduction to H_2 through the thermochemical model on Ni_2P, Fe_2P, and NiFeP surface (g) as well as the thermodynamic regulation based on NiFeP/g-C_3N_4 for photocatalytic HER (h). Copied with permission [75]. Copyright 2019, Elsevier.

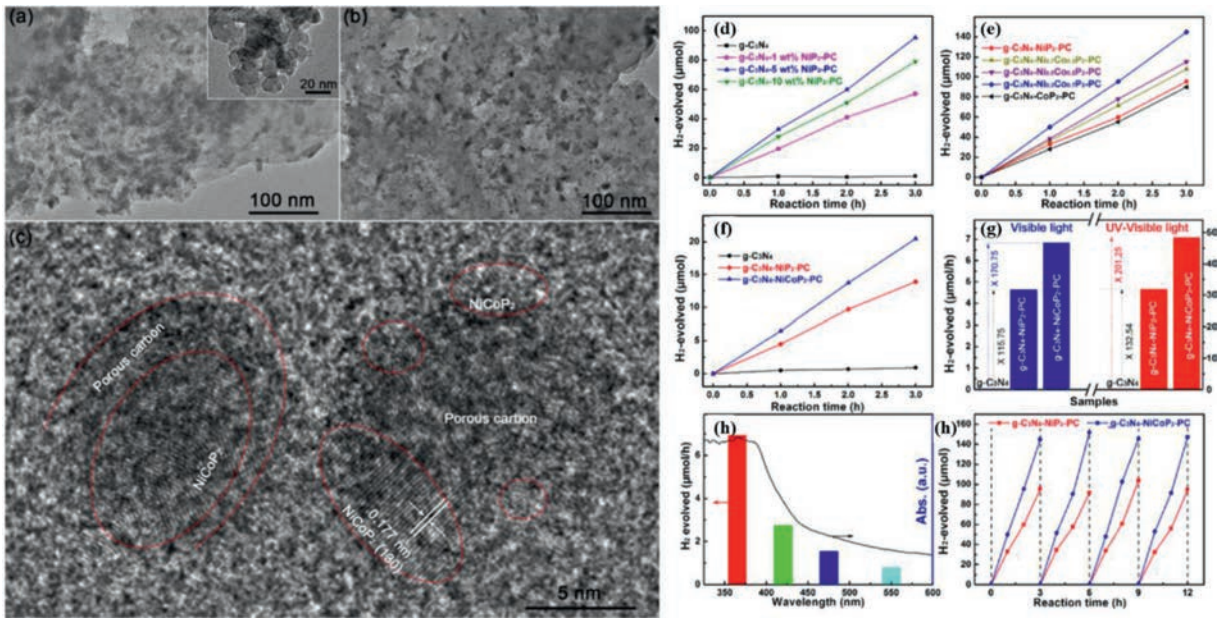

Fig. 6. TEM images of (a) g-C_3N_4-NiCo-MOF, (b) g-C_3N_4-$NiCoP_2$-PC and (c) HRTEM images of g-C_3N_4-$NiCoP_2$-PC. The PHE activities for the as-prepared different photocatalysts in the irradiation of UV-visible light (d-h). Copied with permission [77]. Copyright 2019, ACS.

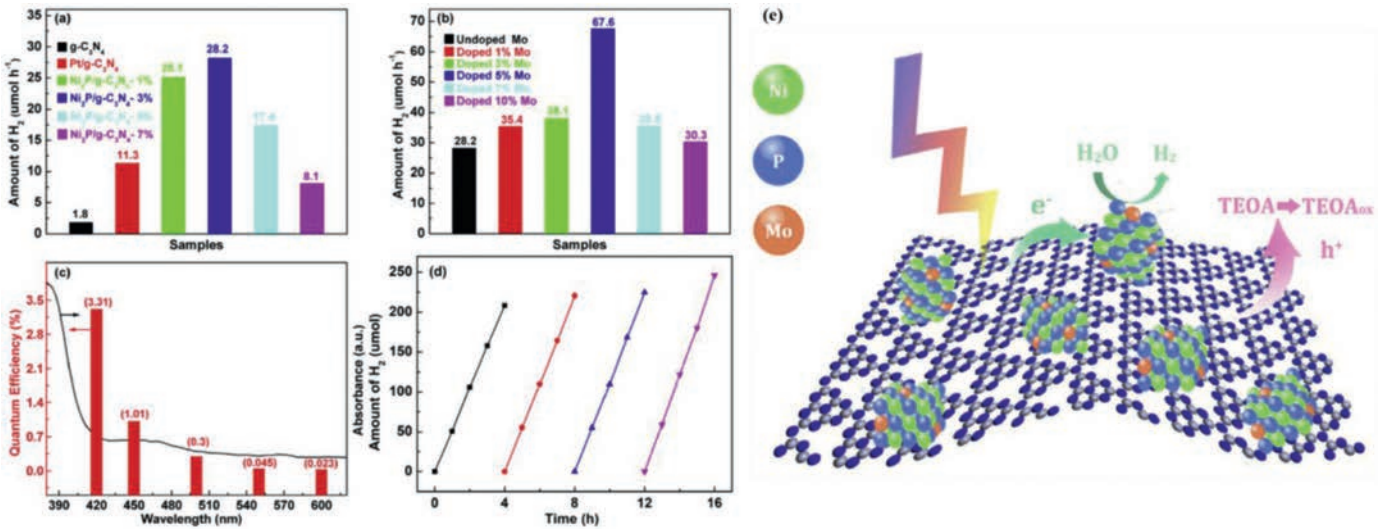

Fig. 7. H_2 evolution rates over $Ni_2P/g\text{-}C_3N_4$ samples with different samples (a,b). Wavelength dependent AQE of H_2 evolution (c), kinetics curves of PHE cyclic reaction (d) and the possible PHE reaction mechanism for Mo-$Ni_2P/g\text{-}C_3N_4$ heterojunction. Copied with permission [66]. Copyright 2020, Elsevier.

under the irradiation of visible light. The quantum efficiency over $g\text{-}C_3N_4{-}NiCoP_2{-}PC$ sample at 420 nm was up to 5.4%, which was at a moderate level among the metal phosphides/$g\text{-}C_3N_4$ as previously reported. Furthermore, the as-prepared photocatalyst exhibited favorable PHE stability over 12 h. More importantly, the optimal PHE performance in pure water is 5.8 μmol h^{-1} g^{-1} in the UV–visible light along with stoichiometric H_2O_2 generation over $g\text{-}C_3N_4{-}NiCoP_2{-}PC$ samples. In this PHE reaction system, the porous structure form MOF template restrains the $g\text{-}C_3N_4$ nanosheet accumulation, the $NiCoP_2$ with low PHE overpotential improves the separation and utilization efficiency as well as the PC locating at the interface mediator between $NiCoP_2$ and $g\text{-}C_3N_4$ facilitates the transmission of photogenerated charge carriers. This work plays an exemplificative role in the development of complex co-catalyst based on BMPs in the $g\text{-}C_3N_4$ reaction system.

As for the modification of cocatalysts, our group has also carried out some work, focusing on modification co-catalysts by introducing other metals. We fabricated the Mo-doped Ni_2P nanodots with high dispersion attached on the surface of ultrathin $g\text{-}C_3N_4$ nanosheet [66], exhibiting the apparently more outstanding PHE activity than that the corresponding $Ni_2P/g\text{-}C_3N_4$ and $Pt/g\text{-}C_3N_4$ photocatalyst (Figs. 7a–d). It should be noted that the AQE variation trend in accordance with the spectral absorption curve well over Mo-$Ni_2P/g\text{-}C_3N_4$ sample and the highest AQE value is 3.31% at 420 nm. Importantly, even the light absorption wavelength at 600 nm, the AQE is still up to 0.023%, which proves that the as-prepared photocatalyst possesses the superior visible-light utilization capacity. Besides, the PHE rates based on Mo-$Ni_2P/g\text{-}C_3N_4$ sample have hardly any reduction after four cycles, demonstrating it has outstanding stability and reusability for meeting practical application. Based on the above analysis, the possible photocatalytic reaction mechanism was obtained. As displayed in Fig. 7e, because the composition of the co-catalyst is Mo doped Ni_2P, which can make the electron structure redistributed as well as provide more surface reaction sites. In consequence, under the visible-light irradiation, the electron-hole pair is generated and separated on $g\text{-}C_3N_4$ surface, after that the electrons transfer immediately to Mo-Ni_2P more easily reducing H_2O molecular to generate H_2 due to effective reaction sites. In the meantime, the holes staying on the $g\text{-}C_3N_4$ surface were consumed by TEOA. In addition to this, it is very rewarding in this area that wang and co-workers prepared the C, N co-doped Fe_2P/Ni_2P polyhedrons cocatalysts originating from NH_2-MIL-101(Fe)/$Ni(OH)_2$ for PHE anchored on the $g\text{-}C_3N_4$ surface under visible light [78]. The highest PHE rate over the as-prepared sample was up to 13.81 mmol g^{-1} h^{-1} under the action of dye sensitization. The AQE at 420 nm reached 45.8%. The enhanced PHE activity was attributed to the efficient separation of photoelectrons, more surface reactive active sites and promoted water reduction reactions on the C, N co-doped Fe_2P/Ni_2P co-catalysts. This work developed new strategies for utilization of MOF-derived cocatalyst for high effective PHE from water splitting.

Non-stoichiometric BMPs have also be proved to act as effective cocatalyst in $g\text{-}C_3N_4$ reaction system. Wang and co-workers prepared 0D/2D heterojunction photocatalyst by $Mn_{0.67}Co_{1.33}P$ nanodots adhered on the $g\text{-}C_3N_4$ nanosheet [65]. As shown in Fig. 8, the highest PHE rate is 113.1 μmol/h from the $Mn_{0.67}Co_{1.33}P/g\text{-}C_3N_4$-5 sample (the content of $Mn_{0.67}Co_{1.33}P$ is 5%), which is much predominant than that of the optimal $CoP/g\text{-}C_3N_4$, $MnP/g\text{-}C_3N_4$ and $Pt/g\text{-}C_3N_4$ photocatalyst. Moreover, the largest AQE value is up to 4.7% at 420 nm and it also exhibits excellent PHE stability and durability over $Mn_{0.67}Co_{1.33}P/g\text{-}C_3N_4$-5 sample. Such excellent results originate from that modification $g\text{-}C_3N_4$ with $Mn_{0.67}Co_{1.33}P$ nanodots accelerates the absorbing capacity and range of visible light as well as the separation efficiency of photogenerated charge carriers. In addition, ternary composite photocatalyst with non-stoichiometric BMPs as cocatalyst has also been reported. Li *et al.* developed $Co_{1.4}Ni_{0.6}P$ and carbon black co-modified $g\text{-}C_3N_4$ photocatalyst by sonochemical loading and in-situ phosphating strategies [79]. It reveals the efficient and stable PHE activity, and the optimal H_2 production rate is up to 405 μmol h^{-1} g^{-1}. In this PHE reaction system, the synergetic effect between the $Co_{1.4}Ni_{0.6}P$ and carbon black makes the separation and transfer of photogenerated charge carriers and H_2 evolution kinetics improved operatively as well as the visible absorption region broadened, thus the PHE activity was significantly improved.

Bimetallic phosphorus oxides as the novel phosphating material have also attracted attention in the domain of photocatalysis as suitable cocatalyst. For example, Guo and co-workers synthesized amorphous $FeCoPO_x$ nanowires combined with $g\text{-}C_3N_4$ nanosheets photocatalyst, which greatly boosted the PHE activity under visible light [80]. The author emphasizes in depth that the Fe species from $FeCoPO_x/g\text{-}C_3N_4$ has the lower coordination number, which is helpful to form a strong and stable interface effect between the two by forming Fe-N bonds. Furthermore, self-optimized elec-

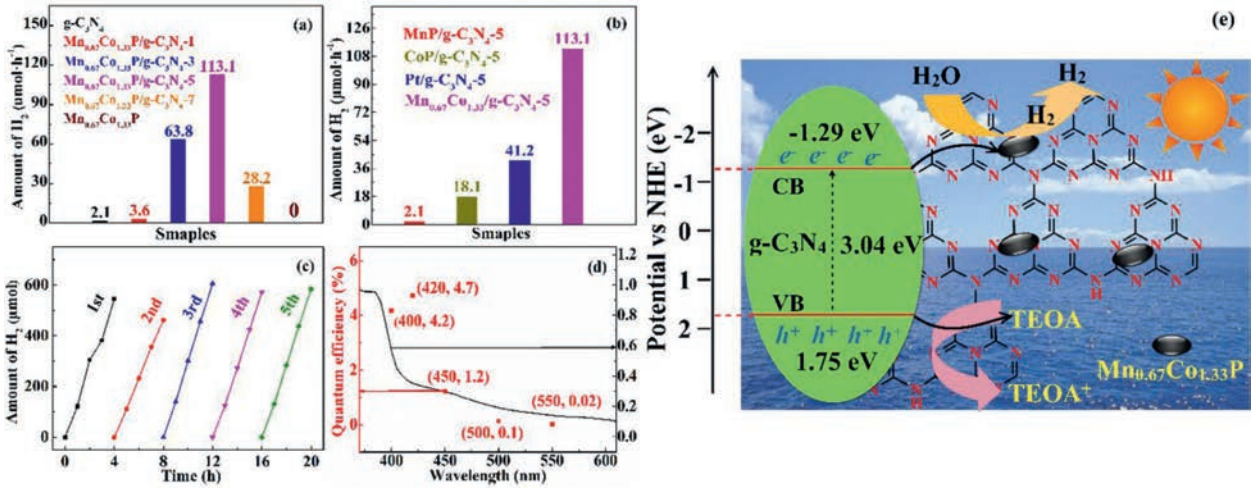

Fig. 8. (a,b) PHE rates based on the different samples. (c) Kinetic curves of H_2 generation in five cycles and (d) QE values over the $Mn_{0.67}Co_{1.33}P$/g-C_3N_4-5 sample along with UV-vis diffuse reflection spectra. (e) Possible mechanism of photocatalytic hydrogen production over $Mn_{0.67}Co_{1.33}P$/g-C_3N_4-5 sample. Copied with permission [65]. Copyright 2019, Wiley-VCH.

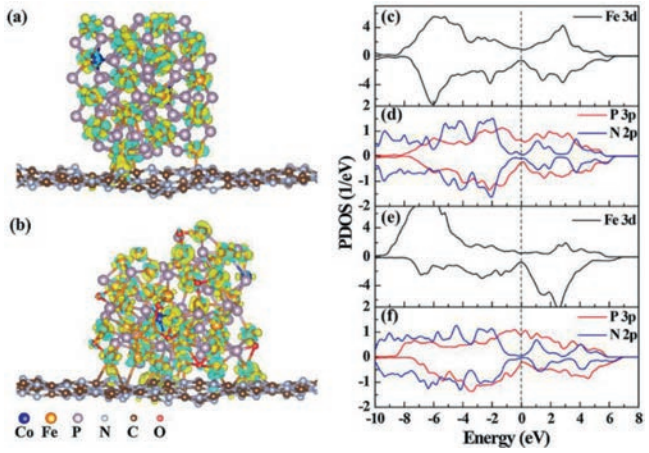

Fig. 9. The charge density difference diagrams of (a) $FeCoPO_y$(NPs)/g-C_3N_4 and (b) $FeCoPO_x$(NWs)/g-C_3N_4. The PDOS plots of the interfacial atoms on $FeCoPO_y$(NPs)/g-C_3N_4 (c and d) and $FeCoPO_x$(NWs)/g-C_3N_4 (e and f). Copied with permission [80]. Copyright 2018, Elsevier.

tronic structure is also conducive to promoting electron transfer from g-C_3N_4 to FeCoPOx through confirmation by first-principles simulation (Fig. 9). The formation of interfacial electronic effect in $FeCoPO_x$/g-C_3N_4 promotes high PHE activity. The summary of PHE performance based on BMPs/g-C_3N_4 photocatalyst is listed in Table 1 [55,56,58–60, 64–66,73–79,81–83].

3.2. BMPs/metal sulfide photocatalyst

In recent years, metal sulfide semiconductor photocatalyst has gained wide attention in the field of PHE application owing to tunable electronics, abundant materials choice, appropriate band location, glorious physical and chemical properties [35,84–86]. We all know that sulfur is an anion combined with a metal cation that may be in monometallic or polymetallic form in metal sulfides. Therefore, large quantities of metallic sulfides have been developed for PHE reaction in recent years, including the common CdS [87], MoS_2 [88], $Zn_xCd_{1-x}S$ [89], $CuCo_2S_4$ [90] and so on. However, the PHE activity of original metal sulfide was not very satisfactory because of their own weaknesses, such as prone photocorrosion, high overpotential, few surface-active sites, low carrier separation efficiency. To overcome those shortcomings, a number of retouching strategies have been developed and utilized. BMPs with unique property as discussed above have also been widely explored to be used for cocatalyst in PHE reaction system over metal sulfide. We will discuss those works in this area detailly.

One of the most representative reports is that Tao and co-works synthetized porous, large-size and ultrathin NiCoP nanosheets along with graphene oxide used as the template through pH-controlled wet-chemical and *in-situ* solid-state phosphating method [91]. By fine-tuning pH from 7.8 to 8.5, the thickness of the obtained NiCoP nanosheets along with the change from 3.5 nm to 12.8 nm (Figs. 10a–d). As the cocatalyst of CdS, the NiCoP/CdS realized ultrahigh PHE rate with 238.2 mmol h^{-1} g^{-1}, which is nearly three times superior in contrast with that of Pt/CdS photocatalyst (81.7 mmol h^{-1} g^{-1}) observed in Fig. 10e. Furthermore, from PL spectra in Fig. 10f, the emission peak intensity of NiCoP/CdS is significantly weaker compared with that of original CdS, which proves the separation efficiency of carriers is obviously boosted and more photoinduced electrons were employed PHE reaction after introducing NiCoP in CdS system. By Mott–Schottky curves and Kelvin probe force microscopy characterization analysis in Fig. 10g and h, the authors confirm the CB potential in CdS is about −0.42 V *vs.* NHE and the work function value of NiCoP is approximate 4.42 eV which is homologous Fermi level of −0.08 V *vs.* NHE, respectively. Thus, the photoelectrons from CdS can be transferred to the surface of NiCoP nanosheets (Fig. 10i), realizing the effective separation and transfer of photoinduced electron-hole pairs. Hence, the typical PHE reaction mechanism over NiCoP/CdS photocatalyst is depicted in Fig. 10j under visible light. There is no more introduction here. Besides, Iqbal obtained superhigh AQE of 76.3% at 420 nm and the best PHE rate of 218 mmol g^{-1} h^{-1} over L-Cysteine capped NiCoP/CdS photocatalyst [92]. The splendid PHE activity was derived from the formation of an intrinsic covalent bond *via* L-Cysteine between CdS and NiCoP as well as abundant surface-active sites. In addition, ternary $Fe_xCo_{1-x}P$/CdS photocatalyst was also prepared for PHE in the irradiation of visible light [54]. The experimental results displayed that the optimal performance of $Fe_{0.4}Co_{0.6}P$/CdS reaches 18.27 mmol h^{-1} g^{-1}, which is much ascendant than that of CoP/CdS and pure CdS. The AQE of $Fe_{0.4}Co_{0.6}P$/CdS is up to 50.6% at 420 nm. Both of which indicate that $Fe_xCo_{1-x}P$/CdS can be considered as higher activity and stability photocatalyst.

Table 1
The PHE performance based on BMPs/g-C_3N_4 photocatalyst.

Photocatalyst	Light source	Sacrificial	Activity(μmol h^{-1} g^{-1})	AQY(%) λ (nm)	Ref.
Zn-Ni-P/g-C_3N_4	λ > 420 nm (LED)	TEOA	10624	23.05 (420)	[55]
NiCo-Pi/g-C_3N_4	λ > 420 nm (Xe)	TEOA	10184	3.9 (440)	[56]
NiCoP@NiCo-Pi/g-C_3N_4	λ > 420 nm (Xe)	TEOA	534.2	9.4 (400)	[58]
Ni_2P/MoP@ g-C_3N_4	λ > 420 nm (Xe)	TEOA	517	5.9 (420)	[59]
NiCoP/g-C_3N_4	UV-vis (Xe)	TEOA	5162	18.5 (400)	[60]
Co_xNi_yP-PCN	λ > 420 nm (Xe)	-	239.3	-	[64]
$Mn_{0.67}Co_{1.33}P$/g-C_3N_4	λ > 420 nm (Xe)	Na_2SO_4	2262	4.7 (420)	[65]
Mo-Ni_2P/g-C_3N_4	λ > 420 nm (Xe)	TEOA	1352	3.31(420)	[66]
NiCoP/g-C_3N_4	UV-vis (Xe)	TEOA	1643	-	[73]
NiCoP/g-C_3N_4	λ > 420 nm (Xe)	TEOA	1430	4.8 (420)	[74]
NiFeP/g-C_3N_4	UV-vis (Xe)	TEOA	3549	4.98 (420)	[75]
NiCoP/g-C_3N_4	300–780 (Xe)	Methanol	159	4.2 (420)	[76]
g-C_3N_4−$NiCoP_2$−PC	UV-vis (Xe)	-	428.9	5.4 (420)	[77]
CN/FeNiP/ g-C_3N_4	λ > 420 nm (Xe)	TEOA	13810	48.5 (420)	[78]
$Co_{1.4}Ni_{0.6}P$/CB/g-C_3N_4	λ > 420 nm (Xe)	TEOA	403	-	[79]
Ru-CoP /GCN NSs	λ > 400 nm (Xe)	TEOA	1172.5	3.49 (420)	[81]
Cu_3P-Ni_2P/g-C_3N_4	UV-vis (Xe)	TEOA	6529.8	18.5 (400)	[82]
Fe_2P-Co_2P/g-C_3N_4	λ > 420 nm (Xe)	TEOA	34700	-	[83]

AQY: Apparent quantum yield. Xe: Xenon lamp. LED: Light emitting diode. TEOA: Triethanolamine.

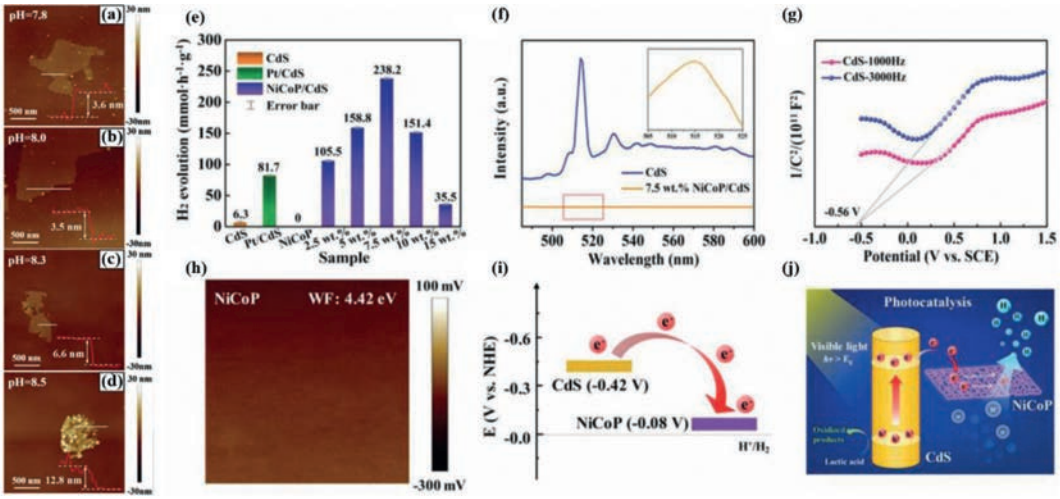

Fig. 10. AFM images of NiCoP nanosheets prepared under different pH values (a–d). Hydrogen production performance over CdS with the different cocatalyst (e). PL spectra of NiCoP/CdS and CdS (f). Mott–Schottky curves of CdS (g). Surface potential diagrams of NiCoP (h). Energy level scheme of NiCoP and CdS (i). The possible photogenerated charge transfer Schematic illustration over NiCoP/CdS under the irradiation of visible light (j). Copied with permission [91]. Copyright 2020, Wiley-VCH.

During the past decades, $Zn_xCd_{1-x}S$ solid solutions have also been widely studied due to the unique and inherent advantages [93]. In what has been previously reported $Zn_xCd_{1-x}S$ solid solutions, $Zn_{0.5}Cd_{0.5}S$ reveals the optimal PHE activity because of its characteristic band gap and CB location. Ge and co-workers synthesized $Ni_xCo_{1-x}P$ nanoparticles groomed $Zn_{0.5}Cd_{0.5}S$ nanorod photocatalysts by in-situ phosphating method [68], where the close connection interface created between the two (Figs. 11a–g). Thus, $Ni_{0.1}Co_{0.9}P/Zn_{0.5}Cd_{0.5}S$ photocatalyst shows the uppermost PHE rate of 976 μmol/h, reaching 11.7 times higher than that of original $Zn_{0.5}Cd_{0.5}S$. The AQE of which is about 19.7% at 420 nm. The PHE activity is still all right going through 16h cycling experiments. The author discussed the possible photocatalytic reaction mechanism in detail based on $Ni_{0.1}Co_{0.9}P/Zn_{0.5}Cd_{0.5}S$ photocatalyst as follows in Fig. 11h, before the two come together, the work function of $Zn_{0.5}Cd_{0.5}S$ is 6.7 eV and $Ni_{0.1}Co_{0.9}P$ is 4.75 eV. The electrons can be transferred from $Ni_{0.1}Co_{0.9}P$ to $Zn_{0.5}Cd_{0.5}S$ on this occasion with the band bending moving down until the both Fermi levels are in accordance to be 6.45 eV in the end. Whereupon, the change of Fermi energy level makes the photoinduced electrons located at the CB of $Zn_{0.5}Cd_{0.5}S$ are transferred to the Fermi level of $Ni_{0.1}Co_{0.9}P$. As a result, the separation and transfer of photogenerated carriers will be promoted because of the influence of band bending at the interface under visible light. A mass of photoinduced electrons at the $Ni_{0.1}Co_{0.9}P$ as the active sites to participate PHE reaction and the holes in the VB of $Zn_{0.5}Cd_{0.5}S$ will be consumed by scavengers.

In addition to this, Zhao, *et al.* obtained high-efficiency NiCoP/CdS/NiCoPi photocatalyst for PHE reaction by nickel−cobalt hydroxide precursor *in-situ* solid-state phosphating method at low flow inert atmosphere [67]. As described in Figs. 12a-d, the PHE rate of NiCoP/CdS/NiCoPi reaches 80.8 mmol g^{-1} h^{-1} under the irradiation of visible light with lactic acid as sacrificial agent, which is considerably superior to that other pure CdS and single cocatalyst including Pt, NiCoP, NiCoPi, respectively. Such the high PHE activity is because that the synergetic effect of concomitant oxidation and reduction cocatalysts made the photoelectrons and holes consumed efficiently and equally. The greater AQE at 420 nm (45%) as well as excellent stability and durability prove the NiCoP/CdS/NiCoPi has potential for practical application. Interestingly, the author suggests the possible separation of charge carriers between the interfaces of NiCoP/CdS/NiCoPi (Figs. 12e–g). After the formation of NiCoP/CdS/NiCoPi heterojunction, the built-in electric field can be formed between the interfaces of each other,

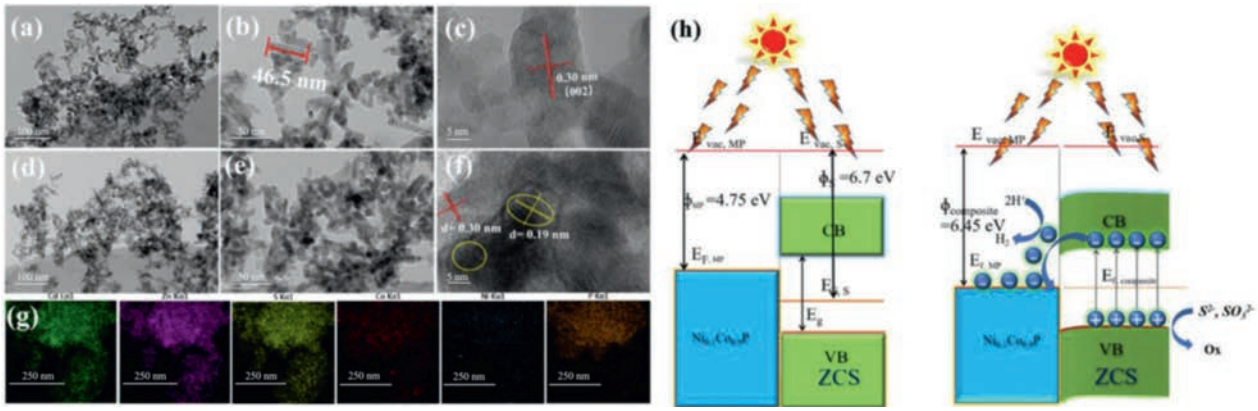

Fig. 11. TEM images of $Zn_{0.5}Cd_{0.5}S$ nanorods (a, b). HRTEM image of $Zn_{0.5}Cd_{0.5}S$ nanorods (c). TEM images and HRTEM image of $Ni_{0.1}Co_{0.9}P$-$Zn_{0.5}Cd_{0.5}S$ (d–f). EDS elemental mapping of $Ni_{0.1}Co_{0.9}P$-$Zn_{0.5}Cd_{0.5}S$ (g). Chart of the band edge locations before and after contact of $Zn_{0.5}Cd_{0.5}S$ and $Ni_{0.1}Co_{0.9}P$ (h). Copied with permission [68]. Copyright 2019, Elsevier.

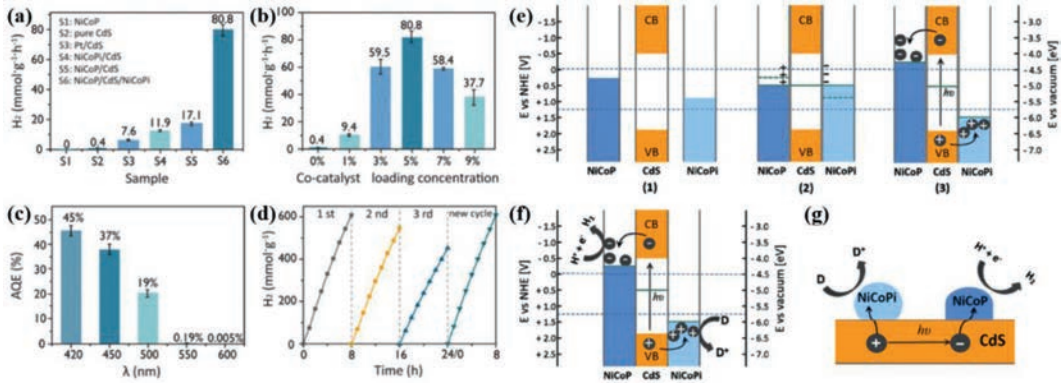

Fig. 12. Various of PHE performance of the as-prepared samples (a-d). Band structures of the prepared samples under thermal equilibrium and the initial stage of photocatalytic process (e). The mechanism of photocatalytic hydrogen production (f,g). Copied with permission [67]. Copyright 2017, ACS.

which can facilitate the photoelectrons migrated *via* heterojunctions, finally realizing thermodynamic equilibrium, and obtaining a novel Fermi energy level. Therefore, CdS nanorods can generate photogenerated charge carriers in the visible light irradiation, afterwards, the electrons can be transferred from CdS to NiCoP which has a lower reduction potential. Meanwhile, the holes are more likely to move from CdS to NiCoPi resulting from its lower oxidation potential. Then, H_2 evolution and sacrificial agent oxidation have occurred on the cocatalysts' surface, thus achieving high-efficient and stable PHE activity from water splitting.

3.3. BMPs/metal oxides photocatalyst

Metal oxides are the first reported semiconductor materials that can be used as photocatalysts. Based on the research so far, the most studied photocatalyst is still TiO_2 for already in practical application [94]. As for TiO_2, its inherent advantages included nontoxicity, non-corrosive, rich source, more stability, simple preparation and so on. However, as everyone knows, those issues of TiO_2 mainly included wide band gap only absorbing ultraviolet light, small AQE due to the easy recombination of photogenerated carriers and low CB reduction potential for water reduction [95]. Many strategies have been exploited to improve its PHE performance and/or the separation efficiency of charge carriers. Hybridization of TiO_2 with BMPs to form composite photocatalysts was regarded as an effective means to overcome the issues raised above. For example, Jing *et al.* used various metal phosphides as cocatalyst for H_2 generation including Ni_2P, NiCoP, and FeP [96]. The experiment results in Fig. 13 show that the NiCoP/TiO_2 composite exhibited the best PHE activity (1.54 mol h^{-1} mg^{-1}), which is higher than that of the Ni_2P/TiO_2 (1.41 mol h^{-1} mg^{-1}), FeP/TiO_2 (0.77 mol h^{-1} mg^{-1}) and pristine TiO_2 nanoparticles (0.11 mol h^{-1} mg^{-1}), respectively. The feasible PHE reaction mechanism has been put forward. It is similar to the described above, under illuminated by ultraviolet light, TiO_2 nanoparticles are excited to generate the corresponding electrons and holes [97]. Then the photoelectrons rapidly transfer to the BMPs as surface-active sites for water reduction to generate H_2. The holes left in the VB of TiO_2 will be consumed by methanol for supplying electrons. It is worth mentioning that the author indicates the one-way migration of photoelectrons makes the Fermi energy level of metal phosphides increase, which is conducive to H_2 evolution.

It is also reported that metal oxide Cu_2O has been proved to act as a very promising photocatalyst for practical application due to its low cost, appropriate band location, unique photophysical properties and so on [98]. Nevertheless, feeblish photostability and low separation efficiency of charge carriers inhibited its applications for PHE reaction. The integration of cocatalyst in to Cu_2O reaction system has effectively reduces the above weaknesses as previous report. BMPs as unique cocatalyst has also been introduced into Cu_2O for high-efficiency PHE activity. As shown in Fig. 14, Liu, *et al.* prepared $Cu_2O/Fe_2P/Ni_3P$ photocatalyst by Fe_2P/Ni_3P as double cocatalyst integrated with Cu_2O nanocubes through the following process [99]. The ultimate PHE rate achieved 108.68 μmol g^{-1} h^{-1}, which is much more splendid than that of primordial Cu_2O. What is even more remarkable is that $Cu_2O/Fe_2P/Ni_3P$ photocat-

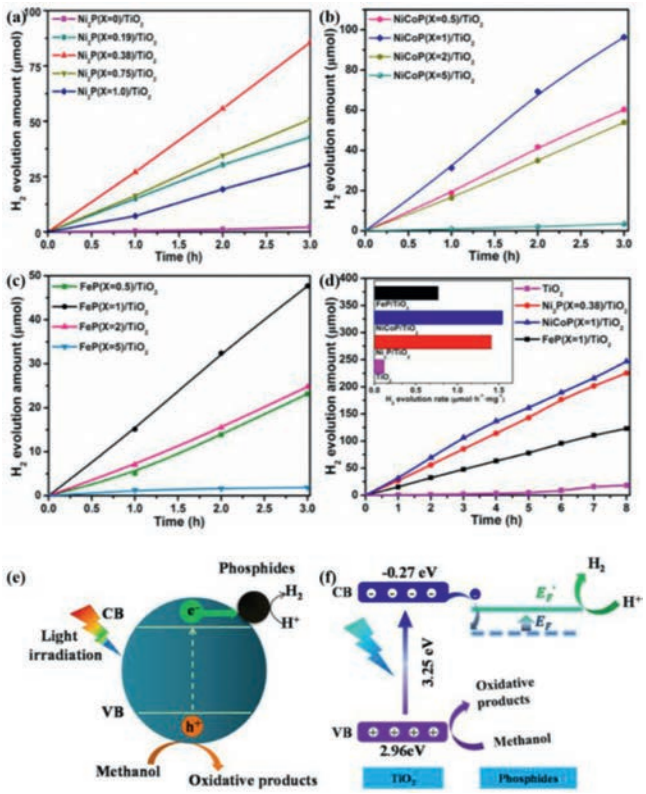

Fig. 13. The PHE activity over the as-prepared photocatalysts with the different amount of Ni_2P (a), NiCoP (b) and FeP (c). The amount contrasts and rate (inset) of H_2 evolution over TiO_2, Ni_2P/TiO_2, FeP/TiO_2 and $NiCoP/TiO_2$ photocatalyst (d). The possible PHE reaction mechanism over metal phosphide/TiO_2 (e, f). Copied with permission [96]. Copyright 2017, Elsevier.

alyst shows a relatively ideal optical stability than that of pure Cu_2O after four PHE reaction cycles. Such faultless PHE activity and stability are because the introduction of Ni_3P/Fe_2P cocatalyst with good conductivity broadened the absorption range of visible light, reduced the recombination probability of photogenerated charge carriers and inhibited the oxidation of Cu_2O effectively. The

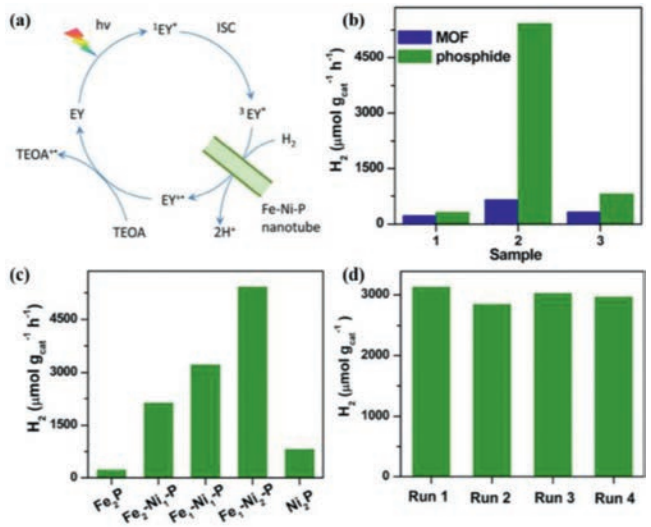

Fig. 15. (a) Mechanism diagram of PHE production by EY dye and Fe-Ni-P nanotubes. (b) PHE production rates of Fe_2P, Fe_1-Ni_2-P and Ni_2P and the corresponding MOF precursors. (c) PHE production rates of Fe-Ni-P catalysts with different compositions. (d) The photostability of Fe_1-Ni_2-P nanotubes. Copied with permission [103]. Copyright 2020, Elsevier.

summary of PHE performance based on metal sulfide/oxides co-catalyzed by BMPs is listed in Table 2 [54,67,68,91,92,96,100,101].

4. BMPs as photocatalyst for H_2 evolution

In addition to use as cocatalyst, Single BMPs has been reported as a photocatalyst to exhibit the high PHE activity under the action of dye sensitization. In the process, photosensitizers play the role of absorbing light and injecting the photogenerated charge carriers to the surface of BMPs photocatalyst as dye-injected charges receptor [102]. The representative work is that Li and co-workers reported the synthesis of bimetallic FeNiP nanotubes catalyst by the metal-organic framework derived manner as well as employing Fe-Ni-MIL-88 nanorods as the template [103]. During the PHE reaction process revealed in Fig. 15a, eosin-Y (EY) was used as photosensitizer to absorb visible light and through the process of intersystem

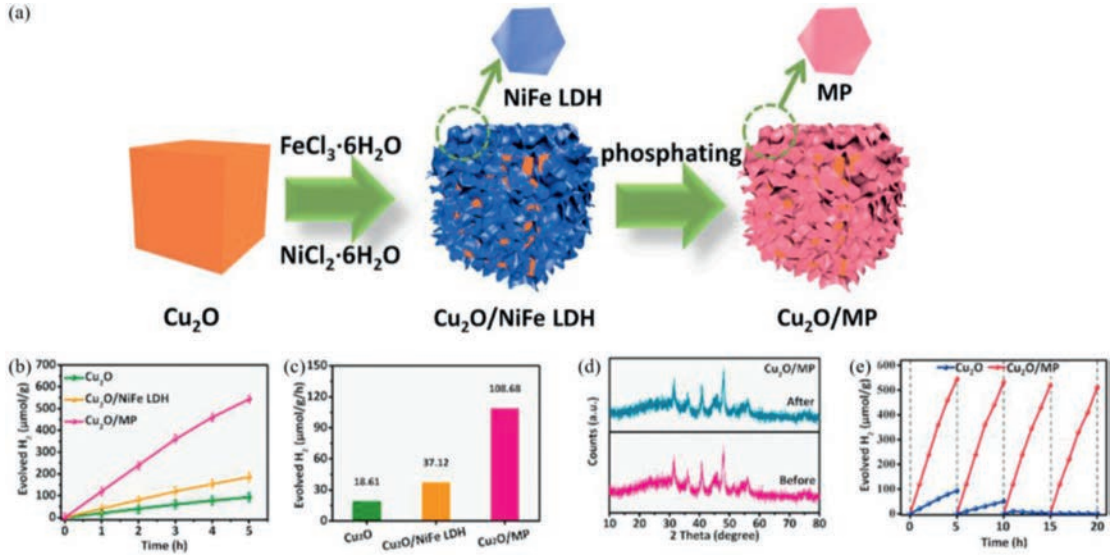

Fig. 14. (a) Schematic diagram of the production of the $Cu_2O/Fe_2P/Ni_3P$ hybrid. (b) Photocatalytic hydrogen production rate of different samples and (c) H_2 production rate of Cu_2O, Cu_2O/NiFe LDH and $Cu_2O/Fe_2P/Ni_3P$; (d) XRD patterns before and after HER, and (e) stability test of $Cu_2O/Fe_2P/Ni_3P$. Copied with permission [99]. Copyright 2021, Elsevier.

Table 2
The summary of PHE performance for metal sulfide/oxides co-catalyzed by BMPs.

Photocatalyst	Light source	Sacrificial	Activity (μmol h^{-1} g^{-1})	AQY (%)/λ (nm)	Ref.
$Fe_xCo_{1-x}P$/CdS	λ > 420 nm (Xe)	$(NH_4)_2SO_3$	18270	50.6/420	[54]
NiCoP/CdS/NiCoPi	λ > 420 nm (Xe)	Na_2SO_4	80800	45/420	[67]
$Ni_xCo_{1-x}P/Zn_{0.5}Cd_{0.5}S$	λ > 400 nm (Xe)	Na_2SO_3/Na_2S	976	19.7/420	[68]
NiCoP/CdS	λ > 420 nm (Xe)	ethanol	218000	76.3/420	[91]
NiCoP/CdS	λ > 420 nm (Xe)	Ethanol	218000	76.3/420	[92]
NiCoP/TiO_2	UV-vis (Xe)	Methanol	1540	-	[96]
ZnCdS–NiCoP	UV-vis (LED)	LA	15794	6.28/475	[100]
NiCoP/CdS	λ > 400 nm (LED)	LA	28412.6	-	[101]

AQY: apparent quantum yield; Xe: xenon lamp; LED: light emitting diode; TEOA: triethanolamine; LA: lactic acid.

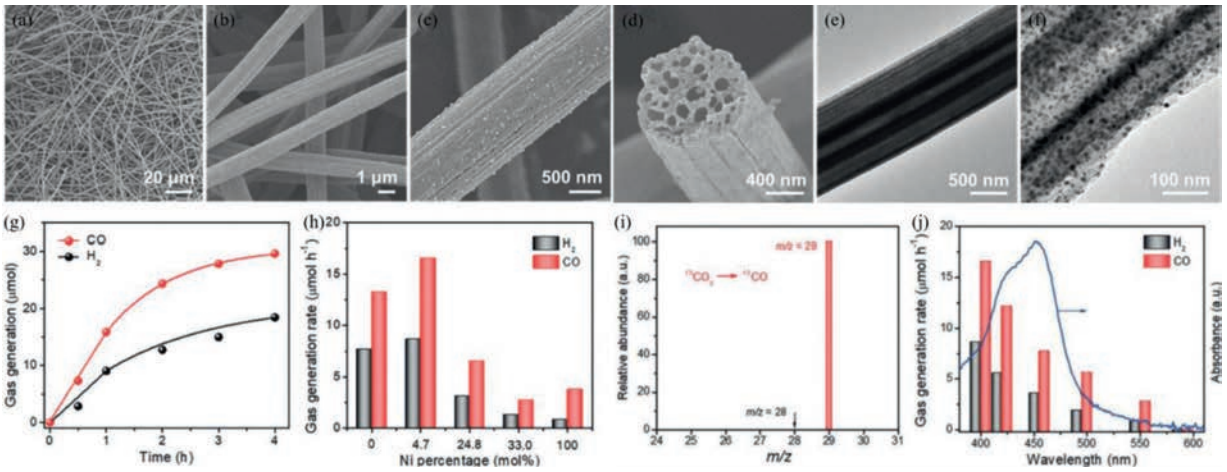

Fig. 16. FESEM images (a–d) and TEM images (e, f) of NiCoOPNPs@MHCFs samples. (g) CO and H_2 production over NiCoOP-NPs@MHCFs sample. (h) Effect of the Ni percentage on the evolution of CO and H_2 in the catalytic process. (i) GC-MS analysis of the generated CO using $^{13}CO_2$ as feedstock. (j) The photocatalytic activity of the NiCoOP-NPs@MHCFs catalyst with wavelength dependent (Ru as photosensitizer). Copied with permission [69]. Copyright 2019, Wiley-VCH.

transition from $^1EY^*$ to $^3EY^*$, it can transfer photoelectrons to Fe-Ni-P nanotubes. Then, after the PHE reaction process over Fe-Ni-P nanotubes, the created EY^{+*} molecules are restored by TEOA using as sacrifice electron donor. The photocatalytic activity is shown in Figs. 15b–d. The PHE rates of all the-prepared phosphides are much higher than their corresponding MOF precursors. And the optimal PHE rate of $FeNi_2P$ is 5420 μmol g^{-1} h^{-1}, which is obviously higher than that of Fe_2P, Ni_2P and another different Fe/Ni ratio phosphide. In addition, the AQE over $FeNi_2P$ photocatalyst comes up to about 15% at a wavelength of 620 nm. Moreover, it also exhibited much stable PHE activity and there is only about 5% decrease activity after five circular reactions. Besides, the Fe-Ni-P nanotubes can also serve as efficient O_2 production photocatalysts through the dye sensitization process, which is not discussed here. What's more, BMPs Co-W-P has also the PHE activity in the dye sensitization reaction system [104]. However, it is unsatisfactory that stability for Co-W-P sample is relatively low mainly because of the leaching of CoP or WP as composition. Besides, a series of metals (Fe, Co, Mn and Mo) were doped into Ni_2P nanoparticles have been prepared through the facile wet-chemical ways [102]. Among those metal-doped Ni_2P, NiMoP nanoparticle exhibits the best PHE activity with the rate of 268 mmol h^{-1} g^{-1} under the $[Ru(bpy)_3](ClO_4)_2$ as photosensitizer in DMF. Whereas, under eosin Y-sensitized PHE reaction system in water, NiCoP nanoparticle shows the optimal PHE rate of 20.4 mmol h^{-1} g^{-1}. Such difference in PHE activity is mainly owing to the different H coverage degrees.

5. Other applications of BMPs as photocatalyst

In addition to applications of BMPs in PHE properties, other photocatalytic applications in a variety of fields have also been reported, including CO_2 reduction, water oxidation, organic pollutants degradation as well as H_2O_2 generation [105–108]. The representative work is that the NiCoOP nanoparticles were limited in the interior of multichannel hollow carbon fibers (MHCFs) to obtain the NiCoOP@MHCFs phototcatalysts for CO_2 reduction [69]. As seen in Fig. 16, the SEM and TEM images confirm that NiCoOP-NPs@MHCFs photocatalyst keeps the interwoven fibrous morphology and NiCoOP NPs with the average size of approximately 10 nm are clearly observed on the surface of the hollow fibrous. The as-prepared NiCoOP-NPs@MHCFs exhibit the very perfect CO_2-to-CO conversion rate as expected under the $[Ru(bpy)_3]Cl_2{\cdot}6H_2O$ as the photosensitizer and the mixture H_2O/triethanolamine/acetonitrile as the reaction media. It is surprising that the amount of photocatalyst is only 0.1 mg, which confirms the mixed metal oxyphosphides has excellent ability for photoreduction CO_2 due to the facilitating of charge transport, regulating of electronic structures and improving of CO_2 adsorption capacity. What is more, Liu and co-workers have prepared the bimetallic Co/Fe phosphide derived from Co/Fe-MOF and inserted in the interior of mesoporous carbon matrix (defined as CoP/Fe_2P@mC) [109]. It exhibits distinctly improved photocatalytic activity for degradation rhodamine B under visible light. This enhanced catalytic activity may result from the synergetic effects of bimetallic phosphates CoP/Fe_2P and mesoporous carbon matrix, the former of which contributes to the interfacial charge transfer and improves the separation efficiency of photogenerated charge carriers as well as the latter has a positive effect on promoting the light adsorption capability. Besides, the TiO_2/FeMnP nanorod with core/shell structure as photoanode for oxygen evolution reaction was obtained successfully, where the rutile TiO_2 was used as core, the FeMnP as interlayer and the $(Mn_{1-x}Fe_x)OOH$ as active surface, as shown in Fig. 17 [110]. The as-prepared catalyst achieves the significant enhancement photoelectrochemical performance and

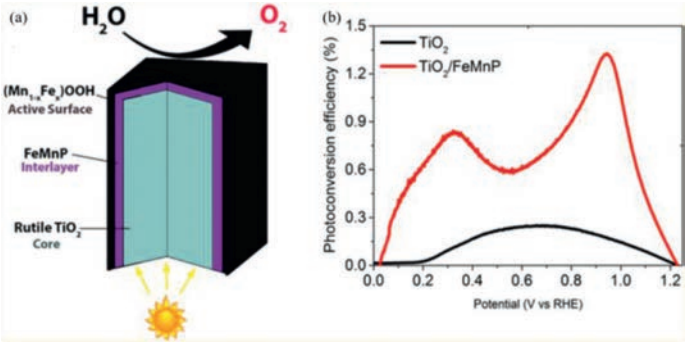

Fig. 17. (a) The as-perpared TiO_2/FeMnP nanorod with core/shell structure as photoanode for oxygen evolution. (b) The Photoconversion efficiency of TiO_2 and TiO_2/FeMnP as a function of applied voltage. Copied with permission [110]. Copyright 2017, ACS.

the photocurrent density is close proximity to the theoretical value of rutile TiO_2 under 100 mW/cm^2 irradiation. Moreover, Fig. 17b shows the optimal photoconversion efficiency of TiO_2/FeMnP (1.33%) is much higher than that of the optimal bare TiO_2 (0.17%) under the same conditions. Such higher photoelectrochemical performance is due to the following two reasons that the FeMnP possess the favorable catalytic activity and stability for oxygen evolution from water splitting as well as the conductive FeMnP interlayer structure between the active sites shell and TiO_2 core as light absorber promotes the interfacial hole transfer capacity and photocarrier collection. The above discussion indicates that bimetallic phosphates can be applied in various photocatalytic applications for satisfying practical application.

6. Conclusion and prospects

In summary, this minireview has summed up the recent research progress of BMPs nanomaterials as cocatalyst for PHE reaction from water splitting. Firstly, we have discussed the existent loading manners of BMPs incorporation with host photocatalysts in detail, including *in-situ* solid-state phosphating method and mechanical mixture loading method. Then, we have investigated the PHE activities of various photocatalysts with BMPs as cocatalyst including g-C_3N_4, metal sulfide, metallic oxide and so on. In those reaction systems, the primary role of BMPs mainly included improving the absorption capacity and broadening the visible-light absorption region, capturing the photoelectron from host photocatalyst to boost the separation efficiency of photogenerated electron-hole pairs as well as providing abundant surface reactive active sites for H_2 evolution. Besides, the current PHE activity comparison over the above-described photocatalysts was analyzed and summarized in detail. After that, we concluded that BMPs can also act as the host photocatalysts in PHE reaction process with the assistance of dye sensitization effect.

Although BMPs as cocatalyst has been made considerable developments in PHE field during the past decades. There remain many challenges and perspectives, which should be proposed for further progress based on BMPs. According to the results of the above summary, some viewpoints are provided as follows:

(1) Most of the reported BMPs show the morphology features of nanoparticles, overlapping and stacking are inevitable existence that reduce the photocatalytic activity. Thus, exploring the suitable methods to prepare other morphology BMPs can be seen as an effective means to boost PHE activity, such as by constructing heterojunction with different morphologies for improving carrier separation efficiency.

(2) The PHE reaction mechanism part is not so clear due to BMPs own deficiency. The effect of the introduced different molar ratios of bimetallic on photocatalytic activity is not explicit put forward, which can be possible plausible explanations by DFT calculation. Moreover, the kind of bimetallic also needs further regulation. Those are also the main work that our group will study in the future.

(3) Compared to a single transition metal phosphide, the type of host catalyst using BMPs as cocatalyst needs to be further developed for obtaining more excellent performance of photocatalyst to meet the practical applications.

(4) Besides BMPs as cocatalyst for PHE reaction, there are few reports on the application of BMPs as cocatalyst in overall water splitting. This should be focused on inquiry in the future. Besides, the scope of other photocatalytic application should be further broadened in the field of photocatalytic CO_2 conversion, photocatalytic degradation of pollutants, photocatalytic H_2O_2 generation and so on.

(5) Furthermore, single BMPs has been used as the main photocatalyst in PHE field, which is summarized in the second half of this minireview. But it only works under dye sensitization which is not conducive to environmental purification. It is desired to seek novel BMPs materials with appropriate band structure for photocatalytic reaction without other force needed.

Nevertheless, even though multifarious challenges must be faced, the potential advantages of BMPs in photocatalysis field is obvious to all. It is very hoped that the minireview can inspire more research interest for developing BMPs nanomaterials for practical and advanced applications in the future.

Declaration of competing interest

The authors declare that they have no known competing financial interests or personal relationships that could have appeared to influence the work reported in this paper.

Acknowledgment

This work was supported by the National Natural Science Foundation of China (No. 52072153), the NSFC-Shanxi Coal Based Low Carbon Joint Fund (No. U1810117), the Natural Science Foundation of Jiangsu Province (No. BK20190867), Key Scientific Research Projects of Colleges and Universities in Henan Province (No. 21A430024), and the Young Talent Cultivate Programme of Jiangsu University (No. 4111310017).

References

[1] F. Zhang, J. Sheng, Z. Yang, et al., Angew. Chem. Int. Ed. 57 (2018) 12106–12110.
[2] D. Zhao, Y. Wang, C. Dong, et al., Nat. Energy 6 (2021) 388–397.
[3] X. Li, C. Huang, W. Han, et al., Chin. Chem. Lett. 32 (2021) 2597–2616.
[4] D. Song, X. Gao, B. Li, et al., Chin. Chem. Lett. 31 (2020) 2483–2486.
[5] C. Li, Y. Xu, W. Tu, et al., Green Chem. 19 (2017) 882–899.
[6] N. Song, S. Hong, M. Xiao, et al., J. Coll. Interface Sci. 582 (2021) 535–542.
[7] Y. Chen, S. Ji, W. Sun, et al., Angew. Chem. Int. Ed. 59 (2020) 1295–1301.
[8] Y. Qin, H. Li, J. Lu, et al., Chem. Eng. J. 384 (2020) 123275.
[9] Y. Xu, J. Xu, W. Yan, et al., Ceram. Int. 47 (2021) 8895–8903.
[10] C. Li, H. Wu, D. Zhu, et al., Appl. Catal. B: Environ. 297 (2021) 120433.
[11] H. Dong, S. Hong, P. Zhang, et al., Chem. Eng. J. 395 (2020) 125150.
[12] F. Wang, Z. Kan, F. Cao, et al., Chin. Chem. Lett. 29 (2018) 1417–1420.
[13] H. Dong, Y. Zuo, N. Song, et al., Appl. Catal. B: Environ. 287 (2021) 119954.
[14] X. Peng, J. Wu, Z. Zhao, et al., Chem. Eng. J. 427 (2022) 130803.
[15] H. Dong, X. Zhang, J. Li, et al., Appl. Catal. B: Environ. 263 (2020) 118270.
[16] L. Mao, X. Cai, M. Zhu, Rare Met. 40 (2020) 1067–1076.
[17] Z. Lu, G. Zhou, M. Song, et al., Appl. Catal. B: Environ. 268 (2020) 118433.
[18] J. Ran, G. Gao, F. Li, et al., Nat. Commun. 8 (2017) 13907.
[19] V. Kumaravel, S. Mathew, J. Bartlett, et al., Appl. Catal. B: Environ. 244 (2019) 1021–1064.
[20] X. Yu, J. Zhang, J. Zhang, et al., Chem. Eng. J. 374 (2019) 316–327.
[21] S. He, C. Yan, X. Chen, et al., Appl. Catal. B: Environ. 276 (2020) 130803.
[22] X. Yuan, D. Shen, Q. Zhang, et al., Int. J. Hydrogen Energy 45 (2020) 9397–9407.
[23] J. Wang, A. Cherevan, C. Hannecart, et al., Appl. Catal. B: Environ. 283 (2021) 119626.

[24] R. Malik, V. Tomer, Renew. Sust. Energ. Rev. 135 (2021) 110235.
[25] M. Zhang, J. He, Y. Chen, et al., Chin. Chem. Lett. 31 (2020) 2721–2724.
[26] H. Dong, N. Song, M. Yan, et al., Chin. Chem. Lett. 32 (2021) 2047–2051.
[27] T. Ouyang, X. Wang, X. Mai, et al., Angew. Chem. Int. Ed. 59 (2020) 11948–11957.
[28] B. Zhang, X. Hu, E. Liu, et al., Chin. J. Catal. 42 (2021) 1519–1529.
[29] H. Dong, M. Xiao, S. Yu, et al., ACS Catal. 10 (2020) 458–462.
[30] Y. Qin, J. Lu, F. Meng, et al., J. Coll. Interface Sci. 586 (2021) 576–587.
[31] Y. Wu, P. Xiong, J. Wu, et al., Nano Micro Lett. 13 (2021) 48.
[32] C. Ji, W. Wang, E.M. El-Sayed, et al., Appl. Catal. B: Environ. 285 (2021) 119782.
[33] X. Zhang, T. Peng, S. Song, J. Mater. Chem. A 4 (2016) 2365–2402.
[34] C. Junze, Q. Lu, M. Zhao, et al., Small 17 (2021) 2006135.
[35] Y. Chen, S. Lan, M. Zhu, Chin. Chem. Lett. 32 (2021) 2052–2056.
[36] J. Li, X. Liu, H. Che, et al., Carbon 172 (2021) 602–612.
[37] Z. Yang, L. Shao, L. Wang, et al., Int. J. Hydrog. Energy 45 (2020) 14334–14346.
[38] M. Zhu, Z. Sun, M. Fujitsuka, et al., Angew. Chem. Int. Ed. 57 (2018) 2160–2164.
[39] L. Ye, C. Han, Z. Ma, et al., Chem. Eng. J. 307 (2017) 311–318.
[40] Z. Sun, M. Zhu, X. Lv, et al., Appl. Catal. B: Environ. 246 (2019) 330–336.
[41] X. Wang, X. Tian, Y. Sun, et al., Nanoscale 10 (2018) 12315–12321.
[42] D. Zeng, T. Zhou, W. Ong, et al., ACS Appl. Mater. Interfaces 11 (2019) 5651–5660.
[43] C. Li, Y. Du, D. Wang, et al., Adv. Funct. Mater. 27 (2017) 1604328.
[44] Z. Lu, C. Li, J. Han, et al., Appl. Catal. B: Environ. 237 (2018) 919–926.
[45] J. Song, C. Zhu, B. Xu, et al., Adv. Energy Mater. 7 (2017) 1601555.
[46] R. Zhang, X. Wang, S. Yu, et al., Adv. Mater. 29 (2017) 1605502.
[47] Y. Tan, H. Wang, P. Liu, et al., Energy Environ. Sci. 9 (2016) 2257–2261.
[48] Q. Mo, W. Zhang, L. He, et al., Appl. Catal. B: Environ. 244 (2019) 620–627.
[49] B. Cao, Y. Cheng, M. Hu, et al., Adv. Funct. Mater. 29 (2019) 1906316.
[50] H. Liang, A. Gandi, D. Anjum, et al., Nano Lett. 16 (2016) 7718–7725.
[51] Y. Pan, K. Sun, Y. Lin, et al., Nano Energy 56 (2019) 411–419.
[52] P. He, X. Yu, X. Lou, et al., Angew. Chem. Int. Ed. 56 (2017) 3897.
[53] C. Hou, Q. Li, C. Wang, et al., Energy Environ. Sci. 10 (2017) 1770–1776.
[54] J. Zhang, Q. Zhao, J. Zhang, et al., Int. J. Hydrog. Energy 45 (2020) 22722–22731.
[55] Y. Li, Z. Jin, L. Zhang, et al., Chin. J. Catal. 40 (2019) 390–402.
[56] Y. Zhang, Y. Dai, L. Yin, et al., Catal. Sci. Technol. 10 (2020) 3654–3663.
[57] Y. Yang, C. Zhou, W. Wang, et al., Chem. Eng. J. 405 (2021) 126547.
[58] Z. Qin, Y. Chen, Z. Huang, et al., J. Mater. Chem. A 5 (2017) 19025–19035.
[59] J. Zhao, B. Fu, X. Li, et al., ACS Appl. Energy Mater. 3 (2020) 10910–10919.
[60] C. Jin, C. Xu, W. Chang, et al., J. Alloys Compd. 803 (2019) 205–215.
[61] L. Hong, R. Guo, Y. Yuan, et al., ChemSusChem 14 (2021) 539–557.
[62] S. Cao, C. Wang, W. Fu, et al., ChemSusChem 10 (2017) 4306–4323.
[63] X. Ren, D. Philo, Y. Li, et al., Coord. Chem. Rev. 424 (2020) 213516.
[64] F. Xue, Y. Si, M. Wang, et al., Nano Energy 62 (2019) 823–831.
[65] J. Wu, C. Li, W. Zhang, et al., Energy Technol. 7 (2019) 1800927.
[66] C. Li, H. Wu, S. Hong, et al., Int. J. Hydrog. Energy 45 (2020) 22556–22566.
[67] Y. Zhao, Y. Lu, L. Chen, et al., ACS Appl. Mater. Interfaces 12 (2020) 46073–46083.
[68] S. Li, L. Wang, N. Xiao, et al., Chem. Eng. J. 378 (2019) 122220.
[69] Y. Wang, S. Wang, X. Lou, Angew. Chem. Int. Ed. Engl. 58 (2019) 17236–17240.
[70] Y. Yang, B. Mao, G. Gong, et al., Int. J. Hydrog. Energy 44 (2019) 15882–15891.
[71] Y. Hong, L. Wang, E. Liu, et al., Inorg. Chem. Front. 7 (2020) 347–355.
[72] L. Wang, Y. Hong, E. Liu, et al., Carbon 163 (2020) 234–243.
[73] L. Bi, X. Gao, L. Zhang, et al., ChemSusChem 11 (2018) 276–284.
[74] C. Li, H. Wu, Y. Du, et al., ACS Sustain. Chem. Eng. 8 (2020) 12934–12943.
[75] Q. Zhu, B. Qiu, H. Duan, et al., Appl. Catal. B: Environ. 259 (2019) 118078.
[76] B. Ma, J. Zhao, Z. Ge, et al., Sci. China Mater. 63 (2019) 258–266.
[77] K. Li, Y. Zhang, Y.Z. Lin, et al., ACS Appl. Mater. Interfaces 11 (2019) 28918–28927.
[78] J. Xu, Y. Qi, C. Wang, et al., Appl. Catal. B: Environ. 241 (2019) 178–186.
[79] R. Shen, W. Liu, D. Ren, et al., Appl. Surf. Sci. 466 (2019) 393–400.
[80] P. Zhou, J. Lai, Y. Tang, et al., Appl. Catal. B: Environ. 238 (2018) 161–167.
[81] S. Meng, P. An, L. Chen, et al., J. Coll. Interface Sci. 585 (2021) 108–117.
[82] W. Sun, Z. Fu, H. Shi, et al., J. Chem. Technol. Biotechnol. 95 (2020) 3117–3125.
[83] L. Cheng, S. Xie, Y. Zou, et al., Int. J. Hydrog. Energy 44 (2019) 4133–4142.
[84] M. Zhu, C. Zhai, S. Kim, et al., J. Phys. Chem. Lett. 10 (2019) 4017–4024.
[85] C. Guo, K. Tian, L. Wang, et al., J. Coll. Interface Sci. 583 (2021) 661–671.
[86] R. Yin, B. Jing, S. He, et al., Water Res. 190 (2021) 116720.
[87] Y. Wang, J. Chen, L. Liu, et al., Nanoscale 11 (2019) 1618–1625.
[88] E. Jiang, N. Song, G. Che, et al., Chem. Eng. J. 399 (2020) 125721.
[89] Z. Han, W. Hong, W. Xing, et al., ACS Appl. Mater. Interfaces 11 (2019) 20521–20527.
[90] H. Li, J. Zhao, Y. Geng, et al., Appl. Surf. Sci. 496 (2019) 143738.
[91] X. Lv, X. Li, C. Yang, et al., Adv. Funct. Mater. 30 (2020) 1910830.
[92] S. Iqbal, Appl. Catal. B: Environ. 274 (2020) 119097.
[93] C. Li, X. Liu, Y. Yan, et al., Chem. Eng. J. 410 (2021) 128316.
[94] I. Shahid, S. Ahmad, N. Shehzad, et al., Appl. Surf. Sci. 523 (2020) 146483.
[95] L. Hua, Z. Yin, S. Cao, Catalysts 10 (2020) 1431.
[96] R. Song, W. Zhou, B. Luo, et al., Appl. Surf. Sci. 416 (2017) 957–964.
[97] D. Li, C. Zhou, Z. Xie, et al., Sol. RRL 5 (2021) 2000813.
[98] T. Zhou, Z. Zang, J. Wei, et al., Nano Energy 50 (2018) 118–125.
[99] S. Liu, J. Huang, H. Su, et al., Ceram. Int. 47 (2021) 1414–1420.
[100] H. Liu, P. Su, Z. Jin, et al., Catal. Lett. 150 (2020) 2937–2950.
[101] L. Song, S. Zhang, J. Ind. Eng. Chem. 61 (2018) 197–205.
[102] H. Man, C. Tsang, M. Li, et al., Appl. Catal. B: Environ. 242 (2019) 186–193.
[103] S. Li, J. Tan, Z. Jiang, et al., Chem. Eng. J. 384 (2020) 123354.
[104] Y. Li, Z. Jin, H. Liu, et al., J. Coll. Interface Sci. 541 (2019) 287–299.
[105] W. Xing, C. Liu, T. Li, et al., J. Alloys Compd. 861 (2021) 158614.
[106] F. Xue, Y. Si, M. Wang, et al., Nano Energy 62 (2019) 823–831.
[107] B. Hu, J. Yuan, J. Tian, et al., J. Coll. Interface Sci. 531 (2018) 148–159.
[108] M. Saruyama, S. Kim, T. Nishion, et al., Chem. Sci. 9 (2018) 4830–4836.
[109] B. Hu, J. Yuan, J. Tian, et al., J. Coll. Interface Sci. 531 (2018) 148–159.
[110] D. Schipper, Z. Zhao, A. Leitner, et al., ACS Nano 11 (2017) 4051–4059.